atmosphere

MDPI

Article

Multi-Scale Ionospheric Anomalies Monitoring and Spatio-Temporal Analysis during Intense Storm

Na Cheng [1], Shuli Song [2,*] and Wei Li [2]

[1] College of Surveying and Geo-Informatics, Shandong Jianzhu University, Jinan 250101, China; chengna@shao.ac.cn
[2] Shanghai Astronomical Observatory, Chinese Academy of Sciences, Shanghai 200030, China; lw@shao.ac.cn
* Correspondence: slsong@shao.ac.cn

Abstract: The ionosphere is a significant component of the geospace environment. Storm-induced ionospheric anomalies severely affect the performance of Global Navigation Satellite System (GNSS) Positioning, Navigation, and Timing (PNT) and human space activities, e.g., the Earth observation, deep space exploration, and space weather monitoring and prediction. In this study, we present and discuss the multi-scale ionospheric anomalies monitoring over China using the GNSS observations from the Crustal Movement Observation Network of China (CMONOC) during the 2015 St. Patrick's Day storm. Total Electron Content (TEC), Ionospheric Electron Density (IED), and the ionospheric disturbance index are used to monitor the storm-induced ionospheric anomalies. This study finally reveals the occurrence of the large-scale ionospheric storms and small-scale ionospheric scintillation during the storm. The results show that this magnetic storm was accompanied by a positive phase and a negative phase ionospheric storm. At the beginning of the main phase of the magnetic storm, both TEC and IED were significantly enhanced. There was long-duration depletion in the topside ionospheric TEC during the recovery phase of the storm. This study also reveals the response and variations in regional ionosphere scintillation. The Rate of the TEC Index (ROTI) was exploited to investigate the ionospheric scintillation and compared with the temporal dynamics of vertical TEC. The analysis of the ROTI proved these storm-induced TEC depletions, which suppressed the occurrence of the ionospheric scintillation. To improve the spatial resolution for ionospheric anomalies monitoring, the regional Three-Dimensional (3D) ionospheric model is reconstructed by the Computerized Ionospheric Tomography (CIT) technique. The spatial-temporal dynamics of ionospheric anomalies during the severe geomagnetic storm was reflected in detail. The IED varied with latitude and altitude dramatically; the maximum IED decreased, and the area where IEDs were maximum moved southward.

Keywords: ionospheric anomalies monitoring; CMONOC; 3D; ROTI; multi-scale; storm

check for updates

Citation: Cheng, N.; Song, S.; Li, W. Multi-Scale Ionospheric Anomalies Monitoring and Spatio-Temporal Analysis during Intense Storm. *Atmosphere* **2021**, *12*, 215. https://doi.org/10.3390/atmos12020215

Academic Editor: Yuichi Otsuka
Received: 21 December 2020
Accepted: 30 Janurary 2021
Published: 4 February 2021

Publisher's Note: MDPI stays neutral with regard to jurisdictional claims in published maps and institutional affiliations.

Copyright: © 2021 by the authors. Licensee MDPI, Basel, Switzerland. This article is an open access article distributed under the terms and conditions of the Creative Commons Attribution (CC BY) license (https://creativecommons.org/licenses/by/4.0/).

1. Introduction

As a significant component of the geospace environment, the ionosphere is a region in the Earth's upper atmosphere at an altitude of 60–2000 km. Generally, it is disturbed and affected unavoidably by space weather or natural disasters [1–3]. Solar activities (e.g., solar flares, solar wind) and geomagnetic storms usually induce ionospheric disturbances. Geomagnetic storms generated by the enhanced solar wind energy can last from hours to days, affecting global dynamics and structures of the ionosphere. These ionospheric anomalies can severely affect various Global Navigation Satellite System (GNSS) applications and radio communication, which relate closely to human space activities [4,5]. The St. Patrick's Day storm occurred on 17 March 2015, which was the most intense geomagnetic storm during Solar Cycle 24 and has become an extensive topic of space weather. Ionospheric disturbances associated with this geomagnetic storm have been studied, such as enhancement/suppression of the equatorial ionospheric anomaly, disturbances in the

polar, and different latitudes' ionospheric analysis [6,7]. Moreover, the ground-based GNSS measurements and GNSS radio occultation data have been used to analyze regional and global ionospheric response to the storm [8,9]. To the best of our knowledge, there has not been a comprehensive study regarding ionospheric anomalies over China.

Monitoring ionospheric anomalies is critical to improve the performance of GNSS Positioning, Navigation, and Timing (PNT) and to provide early warnings of the disaster service during extreme space weather events. Currently, PNT is an obvious developing trend following the GNSS, and the comprehensive PNT system should meet the robust availability, continuity, high accuracy, and reliability [10]. However, with the ionosphere as the main error source, ionospheric anomalies induced by space weather and natural disasters would have severe impacts on the performance of the GNSS. Solar activity induces ionospheric disturbances, which reduce the performance of the GNSS, degrades the accuracy of the GNSS signals, and affects the performance of GNSS broadcast ionospheric models [11,12]. Among ionospheric disturbances, it is generally believed that the ionospheric plasma irregularities can adversely impact GNSS applications through two mechanisms: scintillation and ranging error [13,14]. The current study shows that the positioning errors were doubled when the Global Positioning System (GPS) signals were affected by scintillation during the storm that occurred in September 2017. In addition, ionospheric scintillations induce a considerable clustering effect on the smoothed positioning solution [15]. Therefore, ionospheric anomaly monitoring is significant to improve the various GNSS applications and enhance the reliability of PNT.

With the increase of GNSS stations, the GNSS measurements obtained from the global and regional networks have been widely used to derive the Total Electron Content (TEC) data [16,17]. The Crustal Movement Observation Network of China (CMONOC) GNSS data are available and contribute to characterizing the ionosphere over China. Currently, various kinds of ionospheric monitoring have been achieved based on GNSS measurements from local, regional, or global networks. TEC along with the line-of-sight, two-dimensional Global Ionospheric Map (GIM), and Three-Dimensional (3D) Ionospheric Electron Density (IED) can be obtained. As the TEC of the line-of-sight presents the ionospheric information at Ionospheric Pierce Points (IPPs) with a discrete distribution, it cannot reflect the characteristics of the ionosphere at a large-scale accurately from the aspect of spatial continuity. As regards the ionosphere's modeling at two-dimensional regional or global scales, persistent efforts have been made using observations from the GNSS [18,19]. As is known, the International GNSS Service (IGS) Ionosphere Working Group has been working on ionospheric modeling and preparation for production since 1999, and the GIM (including predict, rapid, final) products are available online [20]. In spite of the high-precision of the GIM, it is unable to represent the spatial structure of the ionosphere precisely, even to characterize its variation over China, since there are few IGS stations there. Hence, reconstructing the 3D ionospheric model is essential to depict the ionosphere, especially for monitoring its anomalies. The Computerized Ionospheric Tomography (CIT) algorithm based on ground-based GNSS, space-borne GNSS, and Low Earth Orbit (LEO) radio occultation measurements has been utilized widely and effectively [21–23]. Therefore, deriving TEC over China and reconstructing the 3D ionospheric model with CMONOC GNSS observations are critical and necessary to monitor ionospheric anomalies. In addition, as a critical ionospheric disturbance index, the Rate of TEC Index (ROTI) has been exploited to investigate the characteristics of traveling ionospheric disturbances, and previous studies have proven it to be an effective method and widely used to characterize the ionospheric scintillation under extreme space weather.

Note that monitoring the ionospheric anomalies during an extreme space weather event is of great significance. The main objective of this study is to monitor ionospheric anomalies based on CMONOC on multiple scales during this storm. The multi-scale ionospheric anomalies' monitoring over China in terms of TEC, IED, and the ROTI is presented and discussed. GNSS observations from CMONOC, the CIT algorithm, and the TEC-derived method are introduced in Section 2. In Section 3, the ionosphere's response to

the storm that occurred on 17–18 March 2015 is investigated by GNSS-derived TEC and the imaged 3D IED model with CMONOC GNSS measurements. The ROTI is utilized to explore the ionospheric anomalies for nighttime as well. Finally, followed by the discussion given in Section 4, concluding remarks are given.

2. Materials and Methods

2.1. Data and GNSS-Derived TEC

In this study, GNSS observations at more than 260 stations from the CMONOC were used to estimate the TEC over China. The geographic distribution of these stations is shown in Figure 1. Ionospheric TEC data were extracted from raw GNSS observations. The measurements P_k, L_k can be expressed as:

$$\begin{cases} P_k = \rho + c \cdot (t_r - t^s) + T + I_k + c \cdot (b_{r,k} + b^{s,k}) + \epsilon_k \\ L_k = \rho + c \cdot (t_r - t^s) + T - I_k + \lambda_k N_k + c \cdot (B_{r,k} + B^{s,k}) + \epsilon_k \end{cases} \quad (1)$$

where ρ denotes the geometric range; λ_k is the wavelength of the carrier; N_k is the integer ambiguity; t_r and t^s represent the receiver and satellite clock offsets, respectively; c is the speed of light; T and I_k denote the tropospheric and ionospheric delay, respectively; the hardware delays in the receiver and satellite are represented by $b_{r,k}$ and $b^{s,k}$; $B_{r,k}$ and $B^{s,k}$ are the hardware delays of the carrier phase for the receiver and satellite; ϵ_k denotes the multi-path and noise; k represents the frequency of GNSS observations.

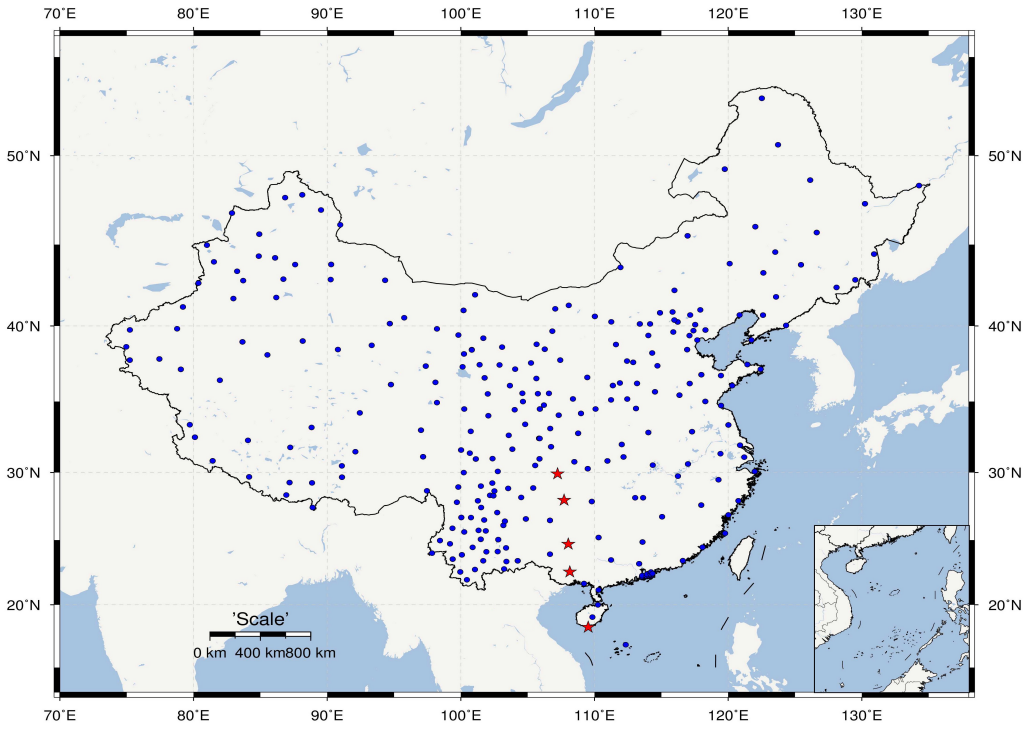


Figure 1. Distributions of the CMONOC GNSS stations (blue dots) and five stations at low latitude (red stars).

At each monitoring station, ionospheric TEC data were extracted from a geometry-free linear combination of undifferenced GNSS pseudo-range and phase measurements. The carrier-to-code leveling method for retrieving ionospheric observables was utilized for an individual satellite implemented in consecutive arcs. For that, it needed to check cycle-slips for in-phase data preprocessing by the TurboEdit algorithm [24]. The expressions for retrieving ionospheric TEC are shown in Equation (2). By using the mapping function, the Slant TEC (STEC) along the path can be transformed into the Vertical TEC (VTEC) at the

IPP. The satellite and receiver Differential Code Biases (DCBs) were obtained from daily DCB products provided by the Shanghai Astronomical Observatory Analysis Center of the International GNSS Monitoring and Assessment System. Note that for this study, the GNSS observation interval was 30 s, and the cutoff for the elevation angle was set to 20° to reduce the influence of measurement errors, especially the multi-path errors.

$$\begin{cases} \widetilde{P}_{4,i,j} = 1/K \cdot STEC + c \cdot (DCB_{r,i,j} + DCB^{s}_{i,j}) \\ STEC = K \cdot [\widetilde{P}_{4,i,j} - c \cdot (DCB_{r,i,j} + DCB^{s}_{i,j})] \\ DCB_{r,i,j} = b_{r,i} - b_{r,j} \\ DCB^{s}_{i,j} = b^{s,i} - b^{s,j} \\ K = -f_i^2 \cdot f_j^2 / [40.3(f_i^2 - f_j^2)] \\ VTEC = STEC \cdot cosz \end{cases} \tag{2}$$

where $STEC$ is the ionospheric TEC along the line-of-sight and f_i and f_j are the GNSS signal frequencies. $\widetilde{P}_{4,i,j}$ is the GNSS combined observation of frequency f_i and f_j. $DCB_{r,i,j}$ and $DCB^{s}_{i,j}$ are the DCBs of GNSS receivers and satellites, respectively. K is a constant coefficient. z is the zenith angle at the IPPs.

2.2. Computerized Ionospheric Tomography

Computerized ionospheric tomography has become one of the most useful for both detecting and monitoring the ionosphere, and it has turned out to be particularly effective for gaining insight into spatio-temporal variations of the ionosphere. It is based on the TEC observations along the radio ray path to inverse the distribution of electron density in the area where the signal is transmitted [21]. The STEC can be defined as the line integral of the IED along the signal path from satellite to ground receiver:

$$TEC = \int_r^s n_e ds \tag{3}$$

where n_e is the electron density and ds denotes the length along the radio ray path. Generally, tomographic algorithms of the ionosphere may be classified into two categories: pixel-based and function-based. Here, we introduce the pixel-based algebraic technique to reconstruct the IED. In order to inverse the spatial and temporal electron density structure from the GNSS TEC observation, we divided the 3D space into small pixels with an altitude from 100 to 1000 km. Furthermore, we assumed the IED in each small pixel was constant during the reconstruction period. The GNSS TEC observation along the ray path from a GNSS satellite to a ground-based receiver can be expressed as:

$$TEC_i = \sum_{j=1}^{n} a_{ij} x_j + e_i \tag{4}$$

in which TEC_i is the TEC along the path i; x_j denotes the IED in pixel j; e_i is the observation noise along the path i; a_{ij} presents the length of path i in pixel j; n is the total number of pixels.

Each voxel of the inversion region is initialized by the International Reference Ionosphere model (IRI) model. The latest IRI-2016 model is adopted to provide the initial IED value for each pixel [25]. The pixel-based algorithm then uses algebraic techniques to distribute the difference between the calculated TEC from the background and the TEC measured by GNSS into the resulting pixel. The Multiplicative Algebraic Reconstruction

Technique (MART) algorithm is used to obtain the IED of each pixel, which can guarantee the non-negative values for electron density [26]. It can be expressed as:

$$X^{k+1} = X^k \left(\frac{TEC_i}{\langle X^k, a_i^T \rangle^2}\right)^{\frac{\lambda_k a_{ij}}{\|a_i\|}} \quad (5)$$

where X^{k+1} is the electron density value obtained from iteration $K+1$; the $\langle X^k, a_i^T \rangle^2$ term is equivalent to a scan through each cell of the ionospheric pixel that calculates the TEC value from the background; a_i^T presents the length of path i; λ_k is a weighting parameter. Generally, the MART reconstruction algorithm can guarantee non-negative values for electron density. Many new iterative algorithms are being developed to improve the algebraic techniques; however, most of them are based on the principles of MART or others [21,23].

2.3. 3D IED Model Reconstruction

To improve the spatial resolution for ionospheric anomalies' monitoring, this study utilized the IED to reflect the ionospheric variations associated with this St. Patrick's Day storm. The 3D IED was reconstructed by the CIT technique, which is presented in Section 2.2. The processing procedures for IED reconstruction in the ionosphere are exhibited in Figure 2.

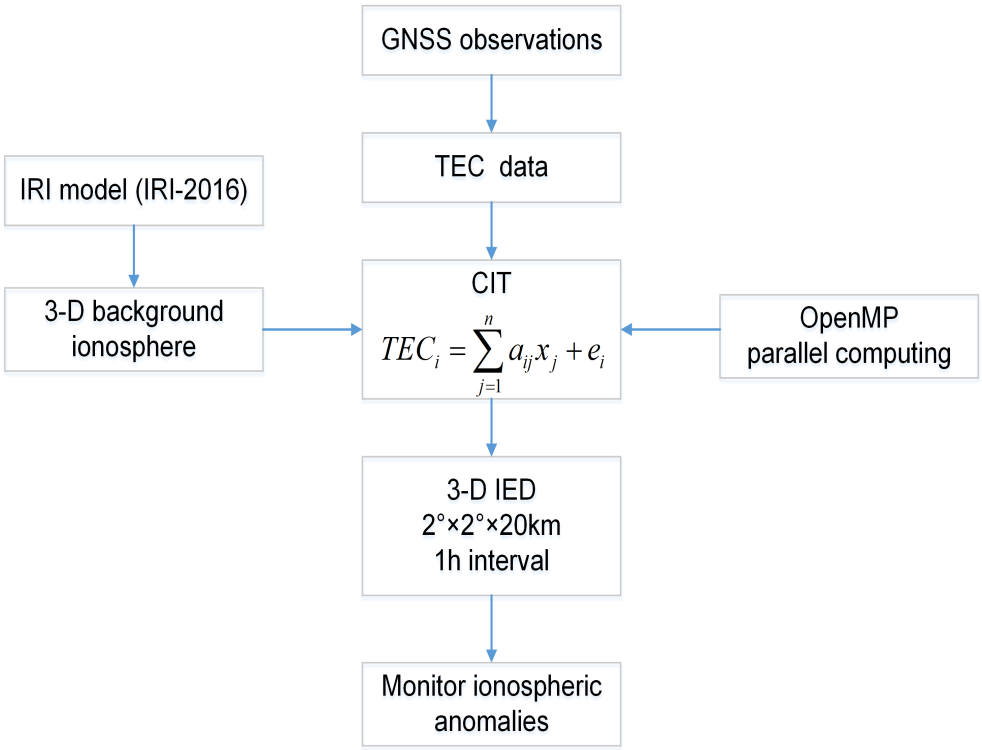


Figure 2. The processing procedures of Ionospheric Electron Density (IED) reconstruction and application. IRI, International Reference Ionosphere; TEC, Total Electron Content; CIT, Computerized Ionospheric Tomography.

Firstly, the TEC derived from the CMONOC GNSS measurements (shown in Equation (1)) need to be prepared for the inversion of IED. Secondly, the ionospheric tomography region should be clarified. In this study, during the reconstructions of 3D IED, the latitude and longitude ranged from 15° N to 55° N and from 70° E to 140° E, respectively, and the altitude ranged from 100 to 1000 km. The inversion region should be discretized into small pixels and the length of the ray calculated through the grid by

the ray-tracing method. The spatial resolution was 2.0° in latitude, 2.0° in longitude, and 20 km in altitude. The time interval was set to 1 h. The latest IRI model (IRI-2016) was adopted to provide the background ionosphere. The IRI-2016 model is being developed to improve the previous algorithm and estimates the initial IED value of each pixel. The latest study provided a valuable tool to improve IRI model performance, updating the IRI background ionospheric mode [27]. Moreover, the effectiveness of data processing should be considered, which relates to the timeliness of ionospheric modeling. Currently, with regard to the large quantity of ground-based GNSS stations from the regional or global networks, massive observations will be available and can be jointly applied in reconstructing the 3D ionospheric model. In view of the data processing efficiency, OpenMP parallelization processing was adopted to improve the ionospheric modeling by making full use of computer hardware resources. The detailed processing strategies of IED reconstruction are summarized in Table 1. We developed the platform for reconstructing the 3D ionospheric model and providing the IED products in near real time. These would be applied to provide space environment information support for spacecraft, space environment anomalies' monitoring, and forecasting. Therefore, the ionospheric anomalies' monitoring during the storm will be conducted and discussed in the following part.

Table 1. Data processing strategies of 3D IED reconstruction. MART, Multiplicative Algebraic Reconstruction Technique.

Items	Strategies
Size	regional-scale
Grid interval	2° (latitude) × 2° (longitude) × 20 km (altitude)
Time interval	1 h
Initial IED value	IRI-2016 model
Derived TEC	dual-frequency GNSS observation (Section 2.1)
Grid distance calculation	three-dimensional ray-tracing
Reconstruction algorithm	MART
Parallel process	OpenMP

2.4. Ionospheric Disturbance Index

The ROTI is used for the characterization of the TEC fluctuation activity, which is correlated with scintillation activity and has been running for several years for real-time detection and monitoring. The ionospheric scintillation means the rapid amplitude and phase variations in the received GNSS signal, which may lead to lines-of-sight of lock for GNSS receivers during extreme ionospheric environment [16,28]. It reflects the ionospheric irregularities and their physical properties. Additionally, ionospheric scintillation depends on multiple factors, such as solar and geomagnetic activity, season, local time, geographical location, and so on [29]. Yang and Liu found that the temporal variations of the ROTI consist of scintillation activity under different ionospheric conditions, and the ROTI has a high correlation relationship with scintillation indices on geomagnetically disturbed days or in solar active months [30]. Therefore, the ROTI derived from GPS dual-frequency measurements is utilized to characterize ionospheric disturbances during the occurrence of this storm in this study. It is also an indicator generally used for quantifying the small-scale ionospheric plasma irregularities. Defined as the standard deviation of the Rate of TEC (ROT, in units of TECU/min), the expressions of the ROTI and ROT are presented in Equation (6).

$$\begin{cases} ROT = \dfrac{TEC(t+dt) - TEC(t)}{dt} \\ ROTI = \sqrt{< ROT^2 > - < ROT >^2} \end{cases} \quad (6)$$

where *ROT* is defined to detect irregular phase fluctuations by measuring the time rate of TEC; *dt* is the time interval between observation epochs and is typically sampled at 30 s. The brackets indicate ensemble averaging.

3. Results

First, as the strongest geomagnetic storm of Solar Cycle 24 so far, the 2015 St. Patrick's Day storm is analyzed in terms of the geomagnetic index. Second, TEC response to the storm is investigated from regional STEC distribution and single-station VTEC variations. Third, the ionospheric disturbance index, ROTI, during this storm is investigated and analyzed. Last but not least, we image the 3D structures of the ionosphere by CIT with CMONOC GNSS measurements and adopt it in monitoring ionospheric anomalies during the 2015 St. Patrick's Day storm.

3.1. Geomagnetic Storm on 17 March 2015

The St. Patrick's Day storm occurred on 17 March 2015, lasting for over 24 h and causing a severe influence on the ionosphere. The Disturbance storm time (Dst) index, planetary geomagnetic disturbance index (which is estimated for three hours), and SYM-Hindex during 14–20 March 2015 are presented in Figure 3. Note that SYM-H index is provided at a 1 min temporal resolution and allows investigating the dynamical changes of the magnetospheric equatorial ring current due to the solar wind parameters' changes [31,32]. Other geomagnetic indices are available online (ftp://ftp.ngdc.noaa.gov/STP/GEOMAGNETIC_DATA/INDICES/). When the Kp index is greater than five, geomagnetic storm alerts will be issued for each occurrence within any 3 h period. It is shown that the storm's sudden commencement occurred at about Universal Time Coordinated (UTC) 04:45 on 17 March 2015, with an abrupt increase of the Kp index from two to five. The main phase began at around UTC 06:00 when the Dst and SYM-H indexes started to gradually decrease. At about UTC 23:00 on 17 March 2015, the Dst index reached its maximum of −223 nT and SYM-H reached −234 nT, indicating that the main phase lasted for about 17 h. After that, the storm went into the recovery phase on 18 March 2015, which lasted for a few more days. This geomagnetic storm was the strongest geomagnetic storm of Solar Cycle 24.

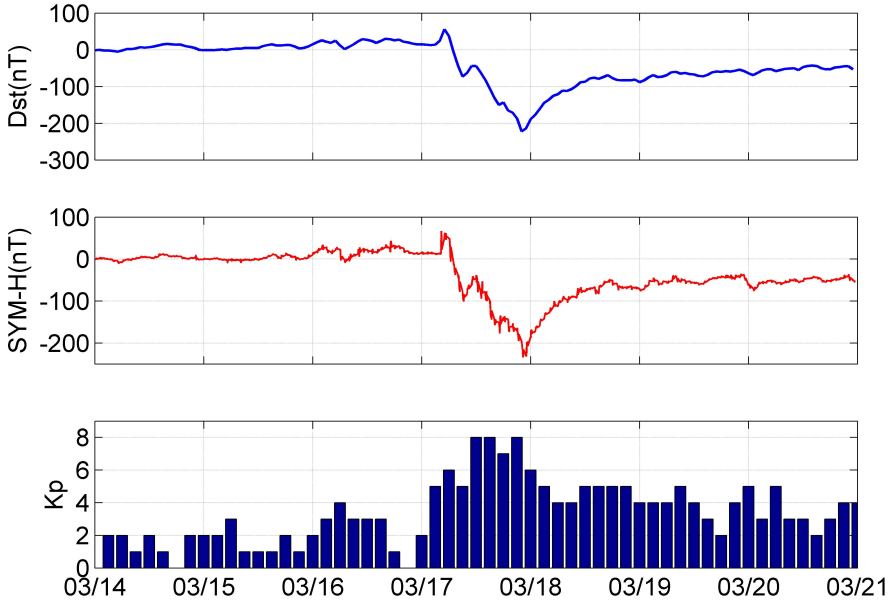


Figure 3. Variations of the geomagnetic parameters (Disturbance storm time (Dst), Kp, and SYM-H index) on 14–21 March 2015.

3.2. TEC Response to the Storm

3.2.1. Regional STEC Variations

Generally, the GNSS-derived TEC is capable of and effective in characterizing the variation of the ionosphere. This study used TEC data derived from more than 260 CMONOC GNSS stations to monitor ionospheric anomalies during the 2015 St. Patrick's Day storm.

Figure 4 shows the spatial-temporal distribution of the ionospheric STEC at the IPPs by GNSS measurements on 17 and 18 March 2015. To distinguish the regional TEC variations between the main phase and recovery phase of this storm, the TEC distribution at three sessions (e.g., UTC 2:00, 12:00, and 20:00) is shown and analyzed. As can be observed at UTC 2:00, the large STEC value at the IPPs distributed in the south of China, especially in southwest China. At the beginning of the main phase of the storm (UTC 6:00–22:00) on 17 March, TEC began to increase, as shown in Figure 4. From UTC 2:00 to UTC 12:00, the significant enhancement of STEC occurred near 20° N; the maximal STEC can up to 200 TECU (1 TECU = 10^{16} electrons/m^2). Until UTC 20:00, the ionospheric TEC decreased and stayed at a low level, the values of which were almost within 50 TECU. Moreover, notable features could be observed until 18 March; a large difference between 17 and 18 March remained regarding STEC; thus the significant STEC decrease occurred on 18 March when the storm was in the recovery phase. There was long-duration depletion in the topside ionospheric TEC during the recovery phase of the storm. Clearly, it can be noted from the distribution of STEC at UTC 12:00 of 18 March that there was no equatorial ionization anomaly phenomenon at the low latitude, and the STEC over China was almost within 50 TECU. In comparison, after UTC 20:00 of 17 March, STEC decreased, and the daily variation of STEC disappeared on 18 March. In addition, corresponding to the occurrence of this storm, it can be found that STEC was enhanced at the beginning of the storm and then decreased significantly, especially during the recovery phase of the storm. It consequently revealed the occurrence of a large-scale ionospheric storm during the storms. This magnetic storm was accompanied by a positive phase and negative phase ionospheric storm.

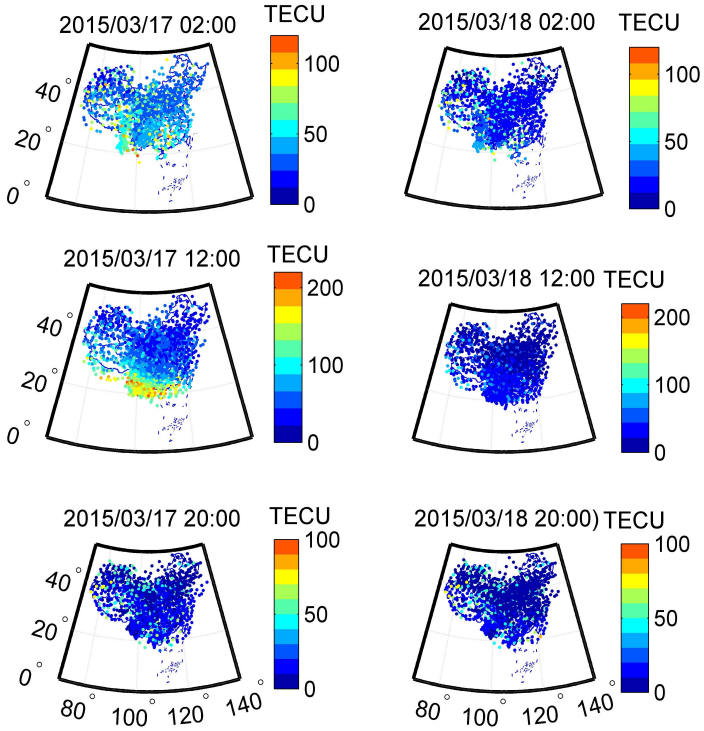


Figure 4. Variations of Slant TEC (STEC) at the Ionospheric Pierce Points (IPPs) at UTC 2:00, 12:00, 20:00 on 17–18 March 2015 (H = 350 km).

3.2.2. Single-Station VTEC Variations

As shown in Figure 4, the TEC at low latitude near 20° N degraded significantly on 18 March, which indicates that the ionosphere was severely affected by the geomagnetic storm. Accordingly, five stations (CQCS, GZFG, GXHC, GXNN, HISY) at low latitude from the CMONOC were selected to analyze the variation of VTEC in detail. VTEC is the projection of STEC on the zenith, which is calculated by the mapping function and the method of weight determining (weighted mean). The geographical location of these five stations is exhibited as red stars in Figure 1. The five sites are just in the northern equatorial anomaly, so they have the favorable condition for the observation to study the VTEC variations and ionospheric scintillation. In order to reflect the spatial and temporal variation of the ionosphere, the variation of the ionospheric VTEC along the longitude of about 108° E during the geomagnetic storm is analyzed and shown in Figure 5. Additionally, the differential VTEC percentage (represented by $PERCENT$) between the value $VTEC_{quiet}$ (16 March) and the daily value $VTEC_{storm}$ (16–21 March) can be calculated by Equation (7).

$$PERCENT = \frac{VTEC_{storm} - VTEC_{quiet}}{VTEC_{quiet}} \times 100\% \quad (7)$$

where $VTEC_{storm}$ presents VTEC during the storm; $VTEC_{quiet}$ denotes VTEC on a quiet day. Except the VTEC on 18 March, it can be observed that the VTEC at the five stations showed consistent and fluctuating daily variations, since the local time at these five stations was similar. Theoretically, the average $PERCENT$ on a quiet day should be around zero, with a continuous trend, and fluctuate randomly within a day. However, the values of $PERCENT$ on 18 March stayed negative entirely and without a daily change, which suggests that these VTECs were lower than those of 16 March. The maximum negative $PERCENT$ can exceed 60% when the storm remains in the recovery phase period. In summary, it is obvious that the ionospheric VTEC and the differential VTEC percentage caused by this storm showed significant abnormality. In other words, VTEC was able to respond to the storm as well.

3.3. Analysis of the ROTI during the Storm

In addition to TEC, the GNSS-derived ROTI was utilized to monitor the ionospheric anomalies during this storm in this study. The ROTI is calculated by GNSS observations at a 30 s rate over 5 min from more than 260 CMONOC GNSS stations, and the elevation mask was set to 20° to minimize multi-path effects. ROTI maps were constructed with a grid of a 2° × 2° resolution. The value in every cell was calculated by averaging all ROTI values covered by this cell area [29].

Existing research results indicated that ionospheric scintillation occurs at night and lasts for a few hours after sunset [33]. Hence, for comparison of the variation of the ROTI between the storm day and the quiet day, three sessions (e.g., UTC 13:00, 17:00, and 21:00) during nighttime were selected and analyzed from 16–18 March 2015. Figure 6 shows the regional maps of the ROTI as a function of geographic longitude and latitude. It presents the spatial and temporal variations of the ionospheric scintillation at night. Many studies have indicated that the ROTI and scintillation indices can be used to investigate middle- and small-scale irregularities at a scale size of a few kilometers and several hundred meters simultaneously [30,34]. Usually, a ROTI $>$ 0.5 TECU/min indicates the occurrence of ionospheric scintillation at scale lengths of a few kilometers [35]. As can be observed from the map of the ROTI in Figure 6, before the storm, the ionospheric scintillations occurred mainly at low latitudes, within 25° N. The ionospheric scintillation activity during the main phase of the magnetic storm showed a general downward trend compared with that before the storm, and the performance in different longitude regions was different. Scintillations were obviously enhanced near 80° E and disappeared completely over South China, where the north crest of the equatorial ionization anomaly was. During the recovery phase, the scintillation phenomenon was particularly suppressed at low latitude regions.

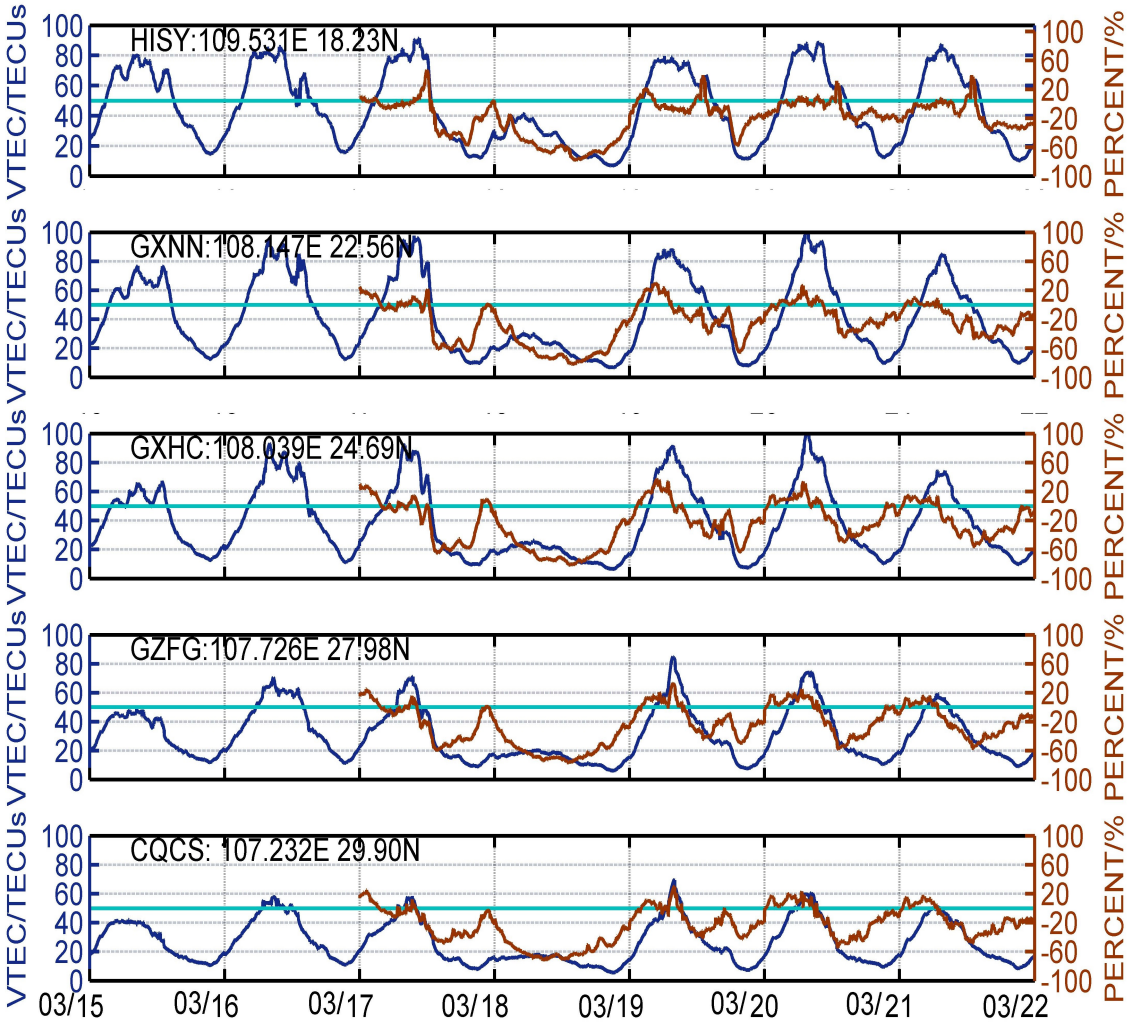


Figure 5. Variations of the VTEC and PERCENT at the low latitude stations of CMONOC.

In addition, by comparing and analyzing the relationship between ionospheric scintillation and VTEC variations, some significant results can be obtained. There was the occurrence of ionospheric scintillation on UTC 13:00, 16 March in Figure 6 corresponding to the second peak in Figure 5, e.g., HISY and GXNN stations, where a big gradient occurred on TEC. While there was the absence of scintillation on UTC 13:00, 17 March indicates the suppression of the storm on TEC to have the second peak corresponding to the curve in Figure 5. The relatively more intense scintillation on UTC 17:00, 17 March compared with that on 16 March indicates the acceleration effect of the geomagnetic storm on the sharp drop of TEC. There was no scintillation on 18 March because of the low and relatively stable level of TEC during the whole day according to the analysis above. During the nighttime of 17 and 18 March, the negative storm and the absence of spread-F and ionospheric scintillation could be caused by the suppression of the eastward electric field after sunset and the equatorward wind surge, which pushed the Equatorial Ionization Anomaly (EIA) towards the Equator [36]. The analysis of the ROTI proved the conclusion above that the storm accelerated the drop of TEC on the latter half-day of 17 March and suppressed the increase of TEC on the forenoon of 18 March in the region of China, that is the storm-induced depletion of TEC, which suppressed the occurrence of the ionospheric scintillation.

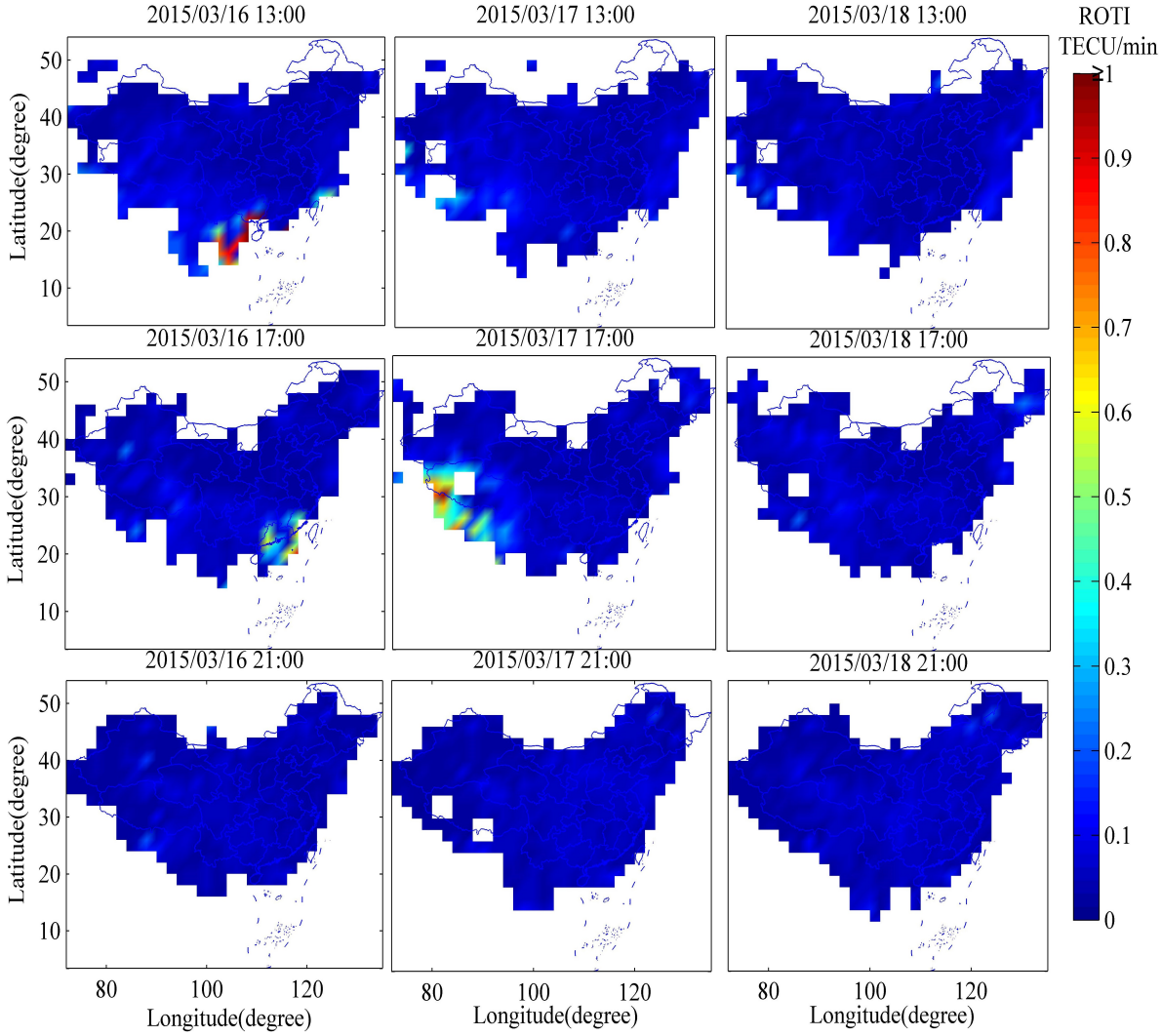


Figure 6. Distribution of the ROTI at UTC 13:00, 17:00, and 21:00 from 16–18 March 2015 (unit = TECU/min).

3.4. 3D IED Response to the Storm

Computerized ionospheric tomography techniques applied to reconstruct the 3D ionospheric model can contribute to many studies of ionospheric dynamics. The objective of this part is to monitor ionospheric anomalies in detail and explore the spatial and temporal features of IED under storm conditions.

As presented in Figure 3, the Dst and Kp index showed generally stable variations on 16 March 2015, which indicates the geomagnetic activity was quiet. Therefore, in order to characterize the features of the ionosphere during this storm, the variations of spatial and temporal IED between the storm day and quiet day are compared. First, the horizontal variations of the ionosphere in the reversion region are analyzed and shown in Figures 7–9. It is noted that the horizontal distribution of IED was mapped onto IPPs at an altitude of 350 km. Figure 7 presents the horizontal distribution of IED at UTC 2:00 from 16–18 March 2015, which correspond to the three panels of the figure, respectively. As can be observed, the horizontal IED from 16–17 March 2015 shows a generally stable variation. In contrast, compared with the IED changes of 16 and 17 March, the variation of the IED on 18 March was more obvious during the storm. As it would be noon according to the local time, the IED stayed at a higher level in most areas of China. In comparison, it can be seen that there was a significant decrease in IED in the same areas.

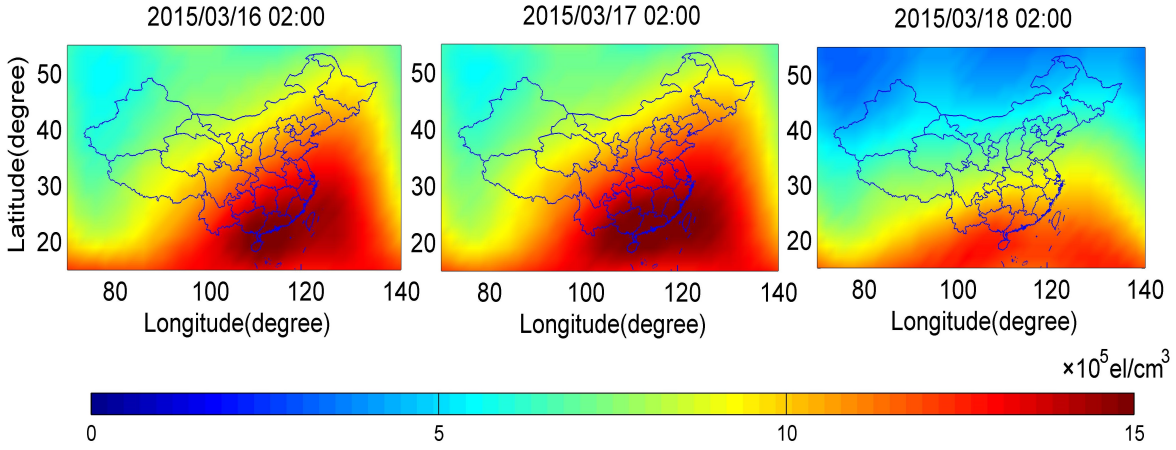


Figure 7. Horizontal distribution of IED at UTC 2:00 from 16–18 March 2015 (H = 350 km).

Figure 8 shows the horizontal variation of the reconstructed IED response to this storm at UTC 12:00 from 16–18 March 2015. Likewise, the variation of the modeled IED behaves smoothly from 16–17 March 2015 and significantly degrades on 18 March 2015. It should be noted that there was an increment in the IED on 17 March, especially in western regions of China. The electric currents are the main drivers responsible for the occurrence of high-latitude enhancements in geomagnetic field variations, such as the development of magnetospheric substorms [37]. Low latitude geomagnetic field variations are related to the occurrence of storms, which are mainly driven by the enhancements of the magnetospheric ring current activity. The positive storm in the low latitude and near the northern EIA was mainly caused by an eastward prompt penetration electric field [36]. At UTC 20:00, it is evident from Figure 9 that the IED on 17 March was lower than 16 March, but this was not as obvious for the IED values on 18 March 2015. Specifically, a significant decrease of the IED occurred on 17 March, especially near the Equator and the high latitude region. It may be suggested that the IED began to decrease from then due to the occurrence of the St. Patrick's Day storm. In other words, the IED can respond to this storm after UTC 20:00 on 17 March, which was consistent with the results for the TEC distribution of IPPs. In general, the results shown in Figures 7–9 indicate that the variations of the reconstructed IED decreased significantly when this storm occurred.

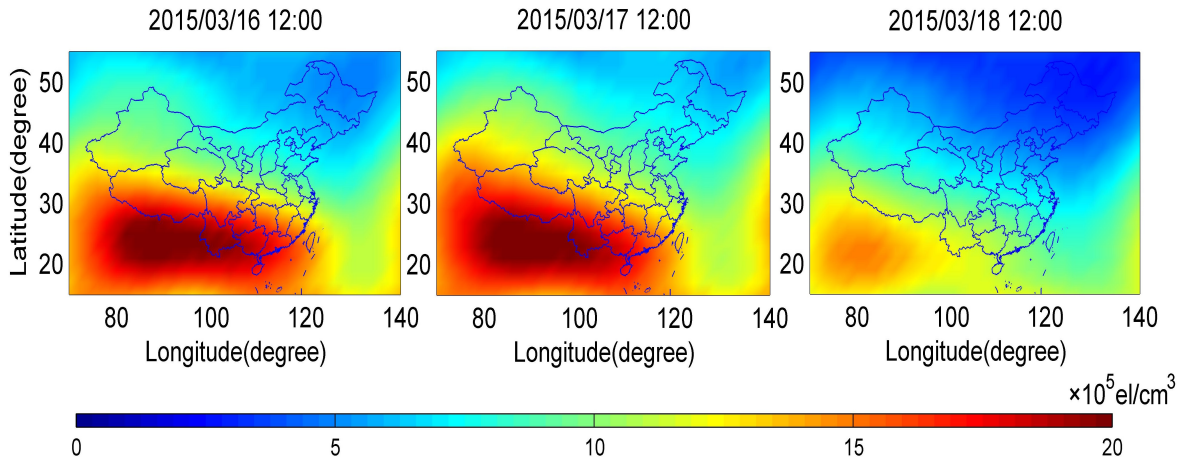


Figure 8. Horizontal distribution of IED at UTC 12:00 from 16–18 March 2015 (H = 350 km).

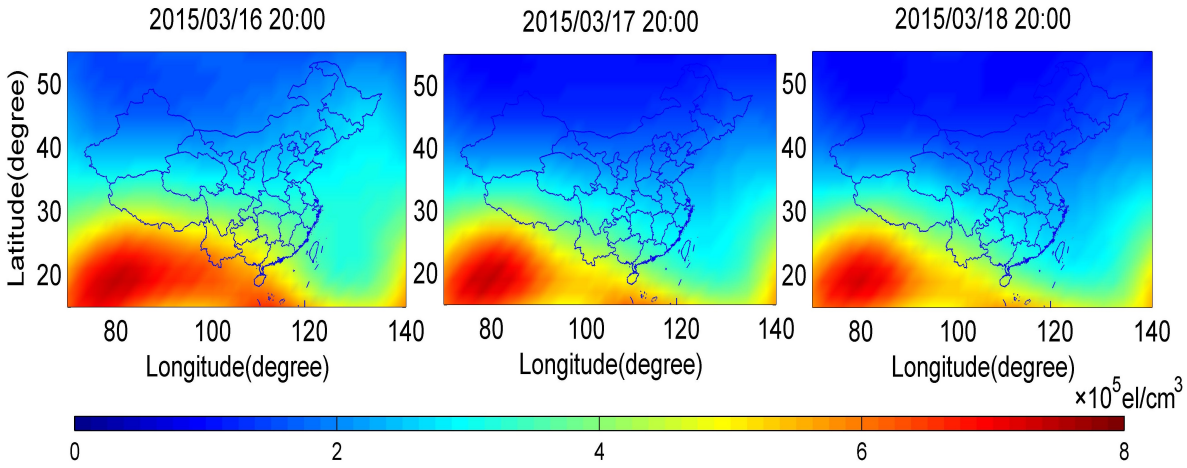


Figure 9. Horizontal distribution of IED at UTC 20:00 from 16–18 March 2015 (H = 350 km).

In comparison, a large decrease occurred on 18 March 2015, presented in the right panel of Figures 7–9. It is clear that the change of the IED in southeast China and northeast China can reach 5×10^5 el/cm^3 and decreases continuously then. Obviously, the IED decreased on 18 March 2015, when the storm stayed in a recovery phase. The long-lasting negative storm during the daytime of 18 March was due to the westward disturbance dynamo electric field, as well as neutral composition disturbances. Generally, the increase and decrease of the IED during the storm typically represent one kind of classification of ionospheric anomalies, known as positive and negative storm effects, respectively. Therefore, from the view of the decrease of the IED, it can be inferred that the St. Patrick's Day storm was a negative storm, and it had a significant impact on the ionosphere.

Following the analysis of the horizontal distribution of the IED, the results of the vertical distribution of the IED during the occurrence of the 2015 St. Patrick's Day storm are analyzed and discussed. The results of the IED along the longitude of 110° E are shown in Figures 10–12, which present the IED variations with altitude and latitude. To compare with the IED under a geomagnetic quiet day, this study exhibits the vertical distribution of IED from 16–18 March 2015. Figure 10 shows the profiles of IED along latitude and altitude at UTC 2:00 from 16–18 March 2015, which correspond to the three panels of the figure, respectively. It can be observed that an equiphase surface is parallel to the Equator at all altitudes. In addition, it is evident from this figure that there are obvious differences in the maximum IED and the area where IEDs are maximum. The area where IEDs are maximum becomes wider from 16–17 March 2015, and the area moves northward, located near 40° N; the maximum IED on 17 March increased with respect to 16 March. On 18 March, the area becomes narrower and moves southward, then the maximum of IED decreases.

Figure 11 illustrates the profiles of the IED along latitude and altitude at UTC 12:00. Clearly, the maximum of the IED and its area show a large difference among the three days. From UTC 2:00 to UTC 12:00, the IED profiles during the main phase of the storm were obviously enhanced. The area where IEDs were maximum became wider from 16–17 March 2015. The maximum IED on 18 March was lower than 16 and 17 March, and the difference could exceed 5×10^5 el/cm^3. The area where IEDs were maximum narrowed down near 20° N. In addition, at latitude region 30° N–55° N, the IED decreased with altitude significantly. Moreover, the results of IED at UTC 20:00 are investigated and shown in Figure 12. As can be observed, the maximum of IED and its area on 17 March is lower than 16 March, but there are no such obvious changes between the results on 17 and 18 March 2015. The area moves southward, and then, the maximum IED decreases on 17 March 2015. In contrast, the profiles of the IED along latitude and altitude from 17–18 March 2015 show a generally stable variation. Moreover, at UTC 20:00 of 17 March, the

IED decreased obviously relative to that of 16 March, especially at the middle and low latitudes. Until UTC 20:00 of 18 March, the TEC profile remained far below the ordinary level, in accordance with the analysis results of the horizontal IED and TEC distribution of IPPs. It can be inferred from the area where IEDs are maximum that the storm affects the ionosphere dramatically at the middle and low latitudes over China.

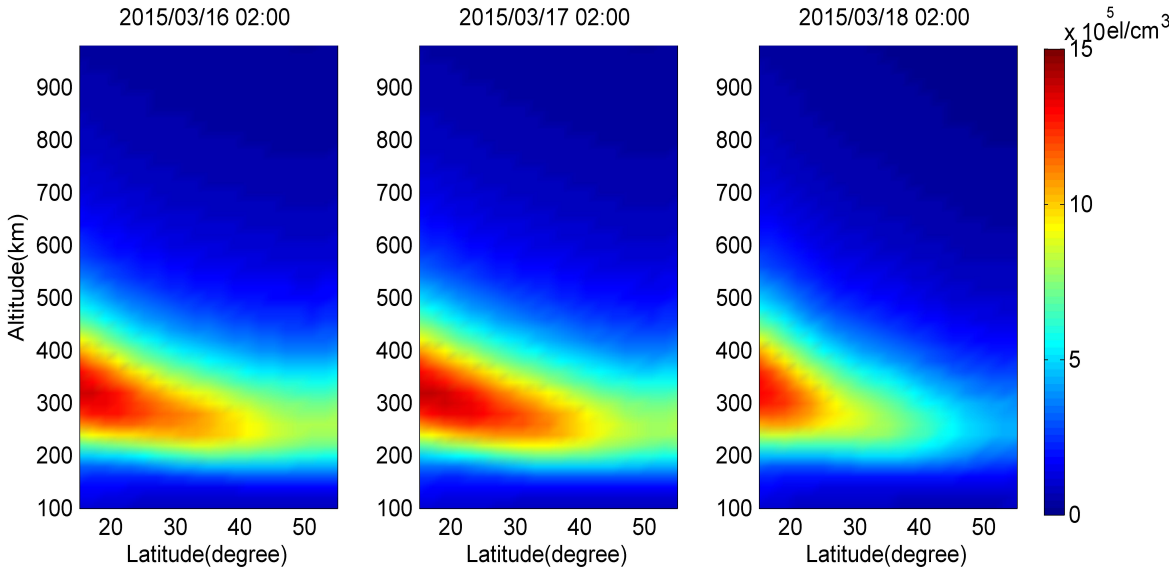


Figure 10. IED profile along latitude and altitude at UTC 2:00 from 16–18 March 2015 (L = 110° E).

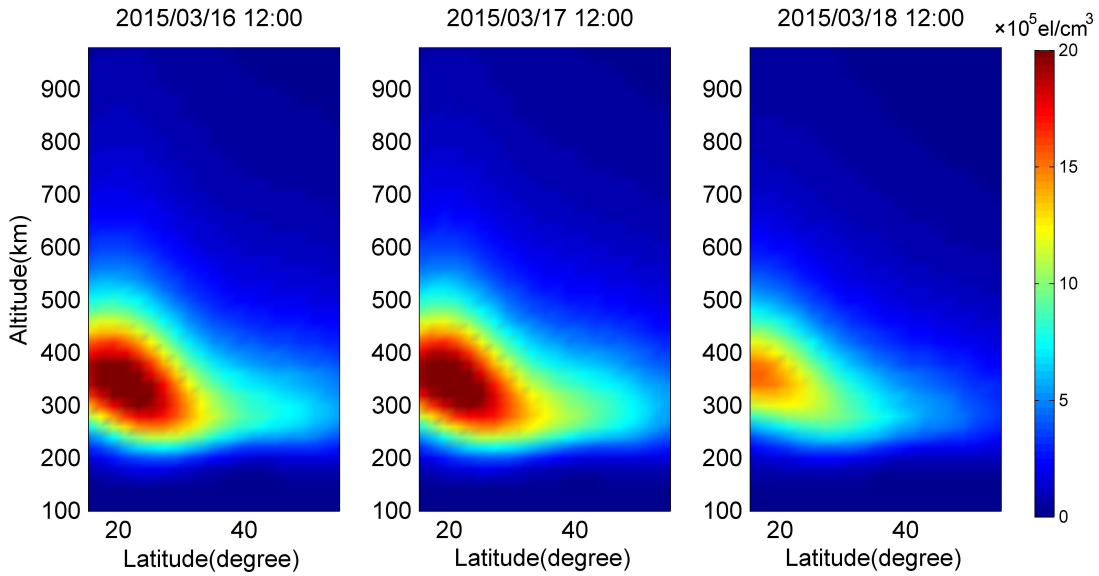


Figure 11. IED profile along latitude and altitude at UTC 12:00 from 16–18 March 2015 (L = 110° E).

In general, by comparison with the variation of the IED from UTC 2:00 to 20:00 on 16 March 2015, at the beginning of the main phase of the magnetic storm, both vertical and horizontal distribution of the IED were significantly enhanced. Then, there was an obvious decrease in the profile of the IED along latitude and altitude for a long duration, especially during the recovery phase of the storm. It can be inferred that this magnetic storm was accompanied by a positive phase and a negative phase ionospheric storm, which accords with the results of TEC. Moreover, the spatial-temporal dynamics of ionospheric anomalies during the severe geomagnetic storm was finely reflected. IED varied with latitude and altitude dramatically; the maximum IED decreased, and the area where IEDs are maximum

moved southward. It also can be found that the peak heights of the electron density of the F2-layer were unchanged during the occurrence of this storm.

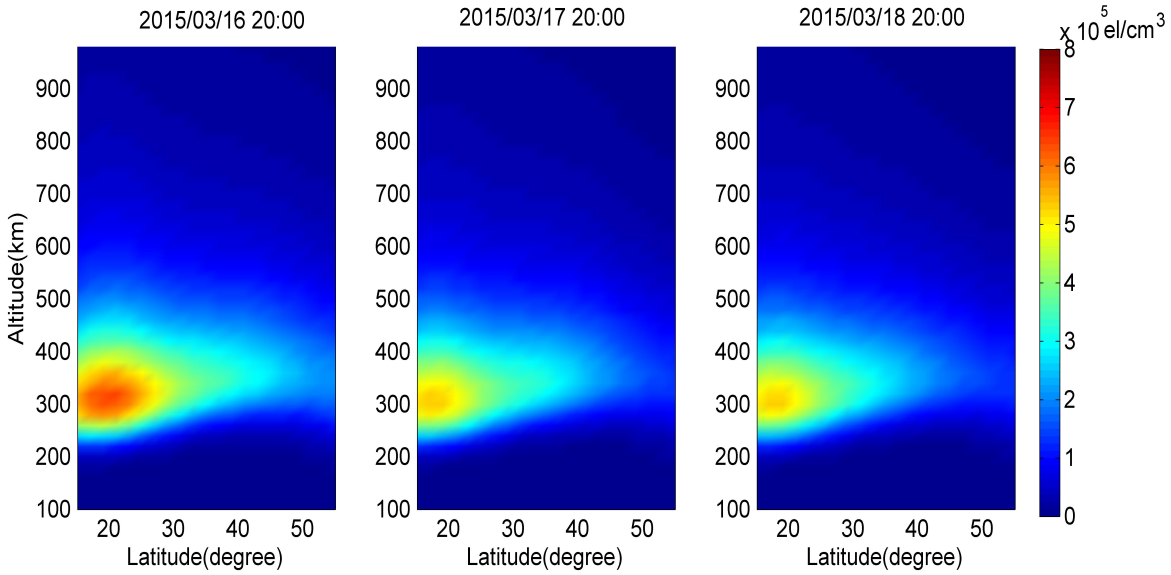


Figure 12. IED profile along latitude and altitude at UTC 20:00 from 16–18 March 2015 (L = 110° E).

4. Conclusions

In this study, multi-scale ionospheric anomalies' monitoring over China is conducted by using CMONOC GNSS data. In view of TEC, the ROTI, and the reconstructed 3D model, the ionosphere response to the St. Patrick's Day storm that occurred on 17–18 March 2015 is investigated and analyzed. It finally reveals the occurrence of a large-scale ionospheric storm and small-scale ionospheric scintillation during the storms, as well as the spatial-temporal dynamics of ionospheric anomalies. The major findings from this study are summarized as follows.

1. To characterize the variation of the ionosphere during this storm, GNSS observations from the CMONOC are applied to derive TEC and the ROTI, and reconstruct the 3D ionospheric model. The multi-scale ionospheric anomalies' monitoring over China in terms of TEC and 3D IED are realized, and the results are consistent. This study also reveals the response and variations in regional ionosphere scintillation. The analysis of the ROTI proves that the storm suppressed the occurrence of the ionospheric scintillation and ionospheric scintillations accompanied by TEC depletions. Specifically, the contribution of the CMONOC observations to ionospheric anomalies' monitoring must be considered in China.
2. For the purpose of determining the effects of this storm on the ionosphere at a 3D scale, the 3D IED is reconstructed by the CIT technique. With respect to the timeliness of modeling, OpenMP parallelization processing is adopted to raise the efficiency in reconstructing the 3D IED model. It can be adopted to achieve the regional-scale or global-scale 3D IED products in near real time on our platform.
3. Based on the reconstructed 3D IED, it consequently reveals the spatial-temporal dynamics of ionospheric anomalies in detail during the severe geomagnetic storm. The magnetic storm was accompanied by a positive phase and a negative phase ionospheric storm. A significant decrease of IED occurred during the recovery phase of the storm, and it totally affected the ionosphere over most parts of China, which is consistent with the results for TEC. Moreover, the IED varied with latitude and altitude dramatically; the maximum IED decreased, and the area where IEDs are maximum moved southward.

In general, this study concerns ionospheric anomaly monitoring, which will contribute to improving the performance of the GNSS under extreme space weather. It also can be applied to provide space environment information support for spacecraft, space environment anomalies' monitoring, and forecasting. As the multi-source measurements rapidly develop, massive data will be available for further ionospheric studies and applications. The rapid development of computer hardware resources and the continuous improvement of high-performance computing methods lay the foundation for reconstructing a 3D ionospheric model in real time. Therefore, further work has to be considered and done. Moreover, the characteristics of the ionosphere correlate to some knowledge of space physics; the exploration of the combination of ionospheric anomalies' phenomena and physical analysis during the storms will be further studied. As ionospheric anomalies during this storm were complex, further studies regarding the ionosphere's response to various storms still need to be carried out.

Author Contributions: S.S. and N.C. conceptualized the study; N.C. developed the algorithm for deriving TEC and reconstructing the 3D ionospheric model based on GNSS observations; W.L. completed the calculation and analysis of the ROTI; N.C. analyzed the obtained results and wrote the manuscript. All authors have read and agreed to the published version of the manuscript.

Funding: This research was funded by the National Key R&D Program of China Grant Number 2016YFB0501503-3, the key project of the National Natural Science Fund Grant Number 41730109, the Doctoral Research Fund of Shandong Jianzhu University, and the Introduction & Training Program of Young Creative Talents of Shandong Province.

Data Availability Statement: The data is supported from "China Earthquake Networks Center, National Earthquake Data Center (http://data.earthquake.cn), and the International GNSS Monitoring and Assessment System (iGMAS) for providing the GNSS observations and products used in this study.

Acknowledgments: The authors would like to acknowledge the data support from "China Earthquake Networks Center, National Earthquake Data Center (http://data.earthquake.cn), and the International GNSS Monitoring and Assessment System (iGMAS) for providing the GNSS observations and products used in this study.

Conflicts of Interest: The authors declare no conflict of interest.

References

1. Yao, Y.; Liu, L.; Kong, J.; Zhai, C. Analysis of the global ionospheric disturbances of the March 2015 great storm. *J. Geophys. Res. Space Phys.* **2016**, *121*, 157–170. [CrossRef]
2. Jin, S.; Jin, R.; Li, J.H. Pattern and evolution of seismo-ionospheric disturbances following the 2011 Tohoku earthquakes from GPS observations. *J. Geophys. Res. Space Phys.* **2014**, *119*, 7914–7927. [CrossRef]
3. Dymond, K.F.; Budzien, S.A.; Nicholas, A.C.; Thonnard, S.E.; Joyce, G. Ionospheric response to the solar flare of 14 July 2000. *Radio Sci.* **2004**, *39*. [CrossRef]
4. Kelley, M.C.; Makela, J.J.; Odile de La, B.; Retterer, J. Convective ionospheric storms: A review. *Rev. Geophys.* **2011**, *49*. [CrossRef]
5. Mao, T.; Sun, L.; Hu, L. A case study of ionospheric storm effects in the Chinese sector during the October 2013 geomagnetic storm. *Adv. Space Res.* **2015**, *56*, 2030–2039. [CrossRef]
6. Jiang, C.; Yang, G.; Liu, J.; Yokoyama, T.; Liu, T.; Lan, T. Equatorial and low-latitude ionospheric response to the 17-18 march 2015 great storm over Southeast Asia longitude sector. *J. Geophys. Res. Space Phys.* **2017**, *122*, 5756–5767. [CrossRef]
7. Nava, B.; Rodríguez-Zuluaga, J.; Alazo-Cuartas, K.; Kashcheyev, A.; Migoya-Orué, Y.; Radicella, S.M.; Amory-Mazaudier, C.; Fleury, R. Middle- and low- latitude ionosphere response to 2015 St. Patrick's Day geomagnetic storm. *J. Geophys. Res. Space Phys.* **2016**, *121*, 3421–3438. . [CrossRef]
8. Liu, J.; Wang, W.; Burns, A.; Yue, X.; Zhang, S.; Zhang, Y. Profiles of ionospheric storm-enhanced density during the 17 March 2015 great storm. *J. Geophys. Res. Space Phys.* **2016**, *121*, 727–744. [CrossRef]
9. Jiao, Y.; Morton, Y.T. Comparison of the effect of high-latitude and equatorial ionospheric scintillation on GPS signals during the maximum of solar cycle 24. *Radio Sci.* **2015**, *50*, 886–903. [CrossRef]
10. Yang, Y.; Li, X. Micro-PNT and Comprehensive PNT. *Acta Geod. Cartogr. Sin.* **2017**, *46*, 1249.
11. Song, S.; Cheng, N.; Xie, H.; Zhou, W. Adaptability of GPS/BDS Broadcast Ionospheric Models to Solar Activities. *Adv. Space Res.* **2019**, *63*. [CrossRef]
12. Cheng, N.; Song, S.; Xie, H. Investigation of Solar Flares Impact on GPS/BDS/GALILEO Broadcast Ionospheric Models. *Radio Sci.* **2018**. [CrossRef]

13. Aarons, J.; Whitney, H.E.; Allen, R.S. Global morphology of ionospheric scintillations. *Proc. IEEE* **1971**, *59*, 159–172. PROC.1982.12314. [CrossRef]
14. Kintner, P.M.; Ledvina, B.M.; Paula, E.R. GPS and ionospheric scintillations. *Space Weather* **2007**, *5*. [CrossRef]
15. Nicola, L.; Alex, M.; Fabio, D.; Luca, S. Effects of Phase Scintillation on the GNSS Positioning Error During the September 2017 Storm at Svalbard. *Space Weather* **2018**, *16*. [CrossRef]
16. Pi, X.; Mannucci, A.J.; Lindqwister, U.J.; Ho, C.M. Monitoring of global ionospheric irregularities using the Worldwide GPS Network. *Geophys. Res. Lett.* **1997**, *24*, 2283–2286. [CrossRef]
17. Mannucci, A.J.; Wilson, B.D.; Yuan, D.N.; Ho, C.M.; Lindqwister, U.J. A global mapping technique for GPS-derived ionospheric total electron content measurements. *Radio Sci.* **1998**, *33*, 565–582. [CrossRef]
18. Yao, Y.; Liu, L.; Kong, J.; Zhai. C. Global ionospheric modeling based on multi-GNSS, satellite altimetry, and Formosat-3/COSMIC data. *Gps Solut.* **2018**, *22*, 104. [CrossRef]
19. Li, Z.; Wang, N.; Wang, L.; Liu, A.; Zhang, K. Regional ionospheric TEC modeling based on a two-layer spherical harmonic approximation for real-time single-frequency PPP. *J. Geod.* **2019**, *93*. [CrossRef]
20. Schaer, S. Mapping and Predicting the Earth's Ionosphere Using the Global Positioning System. *Geod. Geophys. Arb* **1999**, *59*.
21. Tang, J.; Yao, Y.; Zhang, L.; Kong, J. Tomographic reconstruction of ionospheric electron density during the storm of 5–6 August 2011 using multi-source data. *Sci. Rep.* **2015**, *5*, 13042. [CrossRef]
22. Pinto Jayawardena, T.S.; Chartier, A.T.; Spencer, P.; Mitchell, C.N. Imaging the topside ionosphere and plasmasphere with ionospheric tomography using COSMIC GPS TEC. *J. Geophys. Res. Space Phys.* **2016**, *121*, 817–831. [CrossRef]
23. Wen, D.; Liu, S.; Tang, P. Tomographic reconstruction of ionospheric electron density based on constrained algebraic reconstruction technique. *Gps Solut.* **2010**, *14*, 375–380. [CrossRef]
24. Yuan, Y.; Dang, Y.; Cheng, Y.; Zhou, G. Turboedit algorithm and its improvements in ubdifferentiated phase data preprocessing. *J. Geod. Geodyn.* **2009**, *29*, 109–113. [CrossRef]
25. Bilitza, D.; Altadill, D.; Truhlik V.; Shubin, V.; Galkin, I.; Reinisch, B. International Reference Ionosphere 2016: From ionospheric climate to real-time weather predictions. *Space Weather* **2017**, *15*, 418–429. [CrossRef]
26. Raymund, T.D.; Austen, J.R.; Franke, S.J.; Liu, C.H.; Klobuchar, J.A.; Stalker, J. Application of computerized tomography to the investigation of ionospheric structures. *Radio Sci.* **1990**, *25*, 771–789. [CrossRef]
27. Pignalberi, A.; Pietrella, M.; Pezzopane, M.; Habarulema, J.B. Investigating different vTEC calibration methods for data assimilation in ionospheric empirical models. *Adv. Space Res.* **2020**. [CrossRef]
28. Wernik, A.W.; Secan, J.A.; Fremouw, E.J. Ionospheric Irregularities and Scintillation. *Adv. Space Res.* **2003**, *31*, 971–981. [CrossRef]
29. Cherniak, I.; Krankowski, A.; Zakharenkova, I. Observation of the ionospheric irregularities over the Northern Hemisphere: Methodology and service. *Radio Sci.* **2014**. *49*, 653–662. [CrossRef]
30. Yang, Z.; Liu, Z.J. Correlation between ROTI and Ionospheric Scintillation Indices using Hong Kong low-latitude GPS data. *Gps Solut.* **2016**, *20*, 815–824. [CrossRef]
31. Wanliss, J.A.; Showalter, K.M. High-resolution global storm index: Dst versus SYM-H. *J. Geophys. Res. Space Phys.* **2006**, *111*. [CrossRef]
32. Alberti, T.; Lekscha; J.; Consolini, G.; Michelis, P.D.; Donner, R.V. Disentangling nonlinear geomagnetic variability during magnetic storms and quiescence by timescale dependent recurrence properties. *J. Space Weather Space Clim.* **2020**, *10*. [CrossRef]
33. Maski, K.; Vijay, S.K. Analytical study of nighttime scintillations using GPS at low latitude station Bhopal. In Proceedings of the International Conference on Emerging Interfaces of Plasma Science & Technology, Ujjain, India, 9–10 March 2015; doi:10.1063/1.4926701 . [CrossRef]
34. Seif, A.; Abdullah, M.; Hasbi, A.M.; Zou, Y. Investigation of ionospheric scintillation at UKM station, Malaysia during low solar activity. *Acta Astronaut.* **2012**, *81*. [CrossRef]
35. Ma, G.; Maruyama, T. A super bubble detected by dense GPS network at east Asian longitudes. *Geophys. Res. Lett.* **2006**, *33*, L21103. [CrossRef]
36. Sun, W.; Ning, B.; Zhao, B. Analysis of ionospheric features in middle and low latitude region of China during the geomagnetic storm in March 2015. *Chin. J. Geophys.* **2017**, *60*, 1–10. [CrossRef]
37. Kamide, Y.; Kokubun, S. Two-component auroral electrojet: Importance for substorm studies. *J. Geophys. Res. Atmos.* **1996**, *101*, 13027–13046. [CrossRef]